electronic reprint

Journal of
Applied Crystallography
ISSN 0021-8898

Multiple CCD detector for macromolecular X-ray crystallography

Walter C. Phillips, Martin Stanton, Alexander Stewart, Hua Qian, Charles Ingersoll and Robert M. Sweet

Journal of
Applied Crystallography
ISSN 0021-8898

Received 20 September 1999
Accepted 2 December 1999

Multiple CCD detector for macromolecular X-ray crystallography

Walter C. Phillips,[a]* Martin Stanton,[a] Alexander Stewart,[a] Hua Qian,[a] Charles Ingersoll[a] and Robert M. Sweet[b]

[a]Rosenstiel Basic Medical Sciences Research Center, Brandeis University, Waltham, MA 02454-9110, USA, and [b]Brookhaven National Laboratory, Upton, NY 11973, USA. Correspondence e-mail: walter@bug.rose.brandeis.edu

A charge-coupled device (CCD)-based detector designed for macromolecular crystallography is described. The detector has an area of 200 × 200 mm, a readout time of 1.6 s, and total noise equivalent to approximately three 12 keV X-ray photons per pixel. The detector is constructed from a 2 × 2 array of four identical units, each unit consisting of a 4.1:1 demagnifying fiber-optic taper bonded to a 1 k × 1 k, 24 μm pixel, CCD sensor. Each CCD is read out in parallel though four channels and digitized to 16 bits. A Gd_2O_2S phosphor X-ray-to-light converter bonded to an aluminized-plastic film is held in contact with the input surfaces of the fiber-optic tapers with an air pillow. The full width at half-maximum (FWHM) of the point response function is 120 μm, the response is linear to better than 1% over the entire range of intensity from background to nearly full well, the gain is 3.4 e per 8 keV incident X-ray photon, the noise is 12.6 e per pixel for a 10 s integration time, the modulation transfer function (MTF) is 0.35 at 5 line pairs (lp) mm^{-1} (the Nyquest frequency), and the measured detective quantum efficiency (DQE) is 0.74 for relatively strong Bragg peaks. Data collected from crystallographic studies with synchrotron radiation are presented. In an anomalous difference Patterson map for a data set collected in 40 min on a monoclinic myoglobin crystal, the magnitude of the Fe–Fe peaks is 18 times the standard uncertainty of the map.

1. Introduction

In order to build a detector with an area of 400–1000 cm^2, the detector must be constructed from an array of CCDs and demagnifying tapers, given the limited size of commercially available CCDs (25–50 mm) and fiber-optic tapers (135–165 mm diameter). The input surface formed by the faces of the tapers need not be continuous. Multiple-CCD detectors for diffraction applications have been built recently by research groups and commercial manufacturers (Naday *et al.*, 1995; Suzuki *et al.*, 1999; Area Detector Systems Corp., Poway, CA, USA; Molecular Structure Corp./Rigaku, The Woodlands, TX, USA; Oxford Instruments, Oxford, UK). Detectors with smaller areas, employing a single CCD and taper, but otherwise using the same technology, have been built by research groups (Tate *et al.*, 1995; Naday *et al.*, 1994; Stanton *et al.*, 1994) and are now being produced commercially by several companies and are in use for macromolecular crystallography studies at a number of institutions and synchrotron facilities.

General considerations for a crystallography detector include the input area, spatial resolution, sensitivity, noise, dynamic range, pixel size, readout time, reliability and cost. These parameters are interdependent; the choice of each will affect the others. In order to evaluate how performance depends on these parameters, we previously developed general expressions to model the performance of multiple-CCD-based detectors for X-ray crystallography (Stanton, 1993; Stanton *et al.*, 1993). Using these expressions, we predicted that, for a fixed number of CCD sensors, maximizing the area of the detector by using tapers with a demagnification $\gtrsim 4$ would optimize performance for macromolecular crystallography.

In the following sections, we describe the construction of the detector in some detail, present measurements of the performance of the detector, compare these measurements with the performance predicted by calculations, and present the results of data collected from crystallographic studies. Characterization of the detector was conducted with a rotating-anode X-ray source, and crystallographic data were

collected at beamlines X12C and X25 at the National Synchrotron Light Source (NSLS).

2. Description of the detector system

2.1. Basic design

For this multiple-CCD detector, we chose a modular design in which each CCD and taper is enclosed in a vacuum-tight chamber, forming an independent detector module. Four modules are held together in a 2 × 2 array with a mechanical frame, and the array is enclosed in a light-tight hermetically sealed box with a Be input window. An X-ray converter is held in contact with the input surface of the taper array. The modular design allows us to build, test and characterize each module independently. In addition, if a component fails, one module can be removed and replaced without disturbing the others. The CCDs are read out in parallel, and the outputs from each sensor are multiplexed to form a full image. We use 1 k × 1 k, 24 μm pixel, CCD sensors with a taper demagnification of 4.07. Four readout channels are used for each CCD. Four controllers read out, digitize and multiplex the four output channels of each CCD to an interrupt-driven input/output (I/O) computer interface. Data are transferred to four PCs, each receiving data from one module. The four PCs are connected to a 100-Base T Ethernet network. One of the PCs, or another computer on the network, can be used as the master controller for data collection. At the NSLS beamlines where the detector is now operating, data from the four PCs are transferred to a Unix computer which serves as the user interface.

2.2. Mechanical design

The assembled detector camera and the array of four modules are shown in Fig. 1. Each modular unit includes a fiber optic taper, a CCD, a thermoelectric cooling module, a water heat exchanger, and a vacuum-tight housing. A schematic drawing of a module is shown in Fig. 2(*a*), and a schematic drawing of the camera is shown in Fig. 2(*b*).

The square sides of the fiber-optic taper are the limiting lateral dimensions of the module, so that the modules can be butted together to give an essentially continuous input area. We have assembled the modules with a ∼35 μm space between each pair of neighboring tapers in order to allow for small movements of adjacent tapers without direct taper contact. Because the pixel size of 100 μm is considerably larger than the inter-taper space, the image at the taper interfaces is continuous. However, the signal in the row (or column) of pixels at the interface is reduced because the light from some X-ray photons is not collected by the tapers.

In each module, the taper is bonded to an aluminium flange (see Fig. 2). A vacuum-tight chamber enclosing the CCD and heat exchanger is fixed to the flange. The inside volume is evacuated, then filled with Xe gas, and sealed. The CCD is cooled with a two-stage thermoelectric module (Melchor Inc., Trenton, NJ, USA). Thermal contact between the CCD ceramic package and the cold side of the thermoelectric

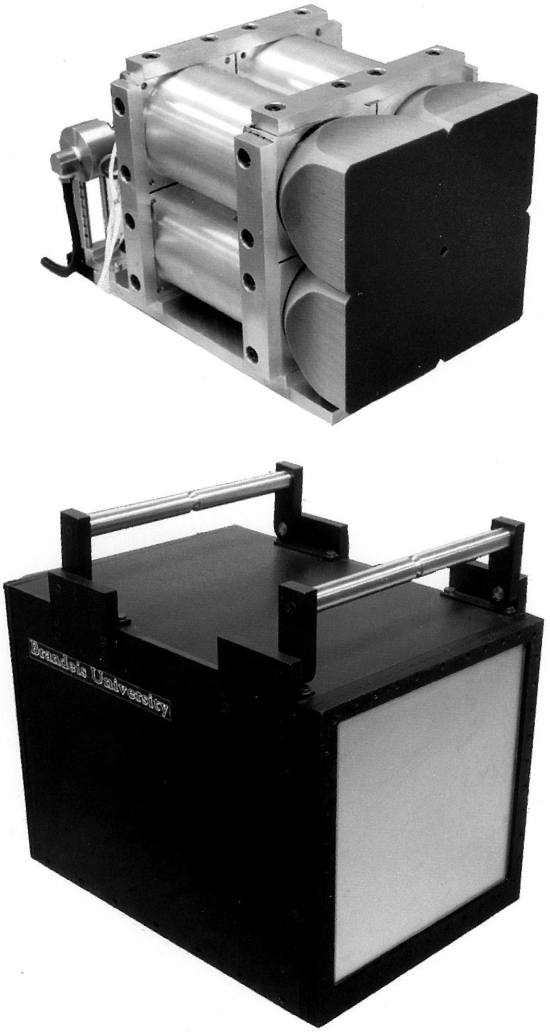

Figure 1
The four-module array (top) and the assembled detector (bottom).

module is provided by a copper ball-and-socket assembly that is held against the back of the CCD package by springs, and allows rotation between the package and the module. The hot side of the thermoelectric module is in contact with an aluminium block that forms a cylinder. A water-filled piston fitted inside the cylinder extracts heat generated by the module. The water is exchanged to an external refrigerated water re-circulator operated at 278 K (Neslab Inc., Portsmouth, NH, USA). The cylinder and piston allow axial motion to compensate for movements caused by thermal expansion and contraction when the assembly is heated and cooled. Thermal contact between the heat-exchanger parts is made using a vacuum-compatible heat-sink compound (Dow Corning 340, Dow Corning, Midland, MI, USA).

Alignment of the 2 × 2 array of modules is provided by an adjustable aluminium frame. Each module functions as a detector. Modules can be operated independently; each can be tested and characterized independently, and a faulty module can be removed and replaced.

The phosphor converter is held in contact with the front surface of the tapers by a permanently sealed, air-filled pillow

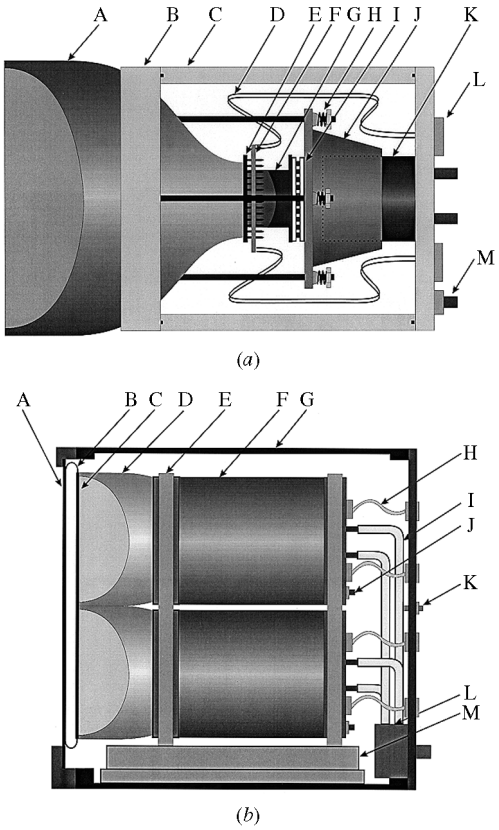

Figure 2
(*a*) Schematic drawing of one module: (*A*) fiber optic taper with 10 × 10 cm front area and 4.1:1 demagnification ratio; (*B*) flange bonded to taper; (*C*) wall of hermetically sealed chamber; (*D*) I/O cables for CCD, (*E*) CCD; (*F*) socket board, (*G*) ball-and-socket heat-transfer coupling; (*H*) ball, spring and nut providing compression force between components; (*I*) thermoelectric cooling module; (*J*) heat-transfer cylinder; (*K*) heat-transfer piston with fittings for circulating water; (*L*) CCD I/O and thermoelectric hermetically sealed connectors; (*M*) pumping port and valve. (*b*) Schematic drawing of the camera showing two modules and the outer housing: (*A*) 0.38 mm Be window; (*B*) pressurized mylar pillow; (*C*) Gd_2O_2S X-ray converter deposited on 0.025 mm aluminized mylar; (*D*) fiber-optic taper; (*E*) bracket coupling modules together; (*F*) inner chamber housing; (*G*) hermetically sealed outer housing; (*H*) cables for CCD I/O, thermoelectric power and temperature sensors; (*I*) cooling water; (*J*) module pumping port and valve; (*K*) housing chamber purge port and valve; (*L*) water distribution manifold; (*M*) base plate.

made from mylar of 25 μm thickness. The pillow is compressed between the beryllium front window, of thickness 0.38 mm, and the converter, maintaining contact between the converter and tapers. When the detector is assembled, the air-tight thermally insulated aluminium housing that surrounds the modules is purged with dry air and then sealed to prevent moisture from condensing on the water tubes and the walls of the modules. By using the pillow and sealing the housing, we have eliminated the need for gas or vacuum lines to the detector. The electronics cable and water connections are located on a removable back plate of the housing.

2.3. Fiber-optic tapers

When the detector was designed, the largest taper available was 135 mm in diameter. By machining the outside cylindrical surface of the taper on four perpendicular planes, a 100 × 100 mm block was cut, forming a square taper (with rounded corners). Butting four of these tapers together allowed us to achieve an area of 200 × 200 mm with small (blank) areas missing at the center, the four corners and four places at the edges (see Fig. 3). We chose this configuration, rather than one using four 95 × 95 mm square tapers, in order to increase the total area by 10%. The choice of how to machine the tapers is a compromise between the total area and the blank areas.

The tapers (supplied by Incom Inc., Southbridge, MA, USA) have a demagnification of 4.07:1, a core to cladding ratio of 70:30, and 5% of the fibers are opaque (EMA), resulting in a light-transmission efficiency of 4%. There are no bevels on the edges of the tapers at the input face, so that a continuous surface is formed between adjacent tapers when they are in contact.

2.4. X-ray converter

The phosphor converter was prepared by settling Gd_2O_2S:Tb (Nichia America, Lancaster, PA, USA) and an organic binder in an organic solution onto an aluminized-mylar film to a density of 13 mg cm^{-2} (∼45 μm thick) (Gruner *et al.*, 1993). The 200 × 200 mm converter is held in intimate contact with the 2 × 2 taper array. The point response function (PRF) profile is determined primarily by light scattering in the converter. Many converters and preparation methods were investigated in order to optimize the profile (see §3.1). In previous detectors, we have deposited the converter directly onto the taper surface (Stanton *et al.*, 1994). However, using that method it was not possible to prepare a uniform phosphor layer out to the edges of the taper, and thus the signal near the interfaces between tapers was degraded.

2.5. CCDs

The CCD sensors are 1024 × 1024, 24 μm pixel, four-output front-illuminated SITe SI003 CCDs operated in multi-pinned phase (MPP) mode (Scientific Imaging Technology Inc., Beaverton, OR, USA). They have a nominal full-well capacity

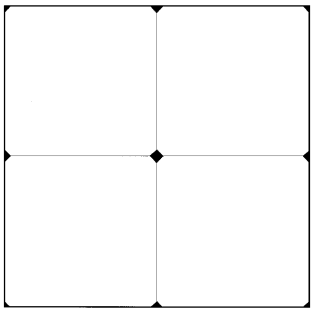

Figure 3
Schematic drawing of the detector input area. Each taper has a small nearly triangular area of ∼4 mm on a side missing at each of the four corners.

of 3.5×10^5 e and an efficiency of ~0.27 e per photon for the predominant 545 nm light component emitted by the phosphor. The silicon sensor is bonded to a ceramic package and its surface is flat to ~2 μm. Each CCD is epoxy-bonded directly to the small end of a taper. The cured bond thickness is approximately 3–5 μm. The CCD/taper assembly can be repeatedly temperature cycled between 293 and 223 K without degradation of the epoxy bond.

2.6. Readout electronics

The CCD integration and readout is controlled by electronics developed by us (Naday *et al.*, 1995). There are four controllers, one for each CCD. Four readout channels are used for each CCD. The controller provides 16 bit digitization at a readout speed of 160 k pixels channel^{-1} s^{-1}. Each controller simultaneously reads out, digitizes and multiplexes the CCD output to an interrupt-driven I/O computer interface. Data are transferred in parallel through a first in first out (FIFO) buffer to four Linux PCs. This gives a total readout time of 1.6 s for the full detector image of $4 \times 1024 \times 1024$ pixels. The four PCs are connected to a 100-Base T Ethernet network. One of the PCs, or another computer on the network, can be used as the master controller for the data collection. At the NSLS, corrected data from the four PCs are transferred in < 1 s to an SGI Unix-based master computer that serves as the user interface.

2.7. Software

Corrections for spatial distortions introduced by the fiber-optic taper, corrections for non-uniform response introduced by the converter, taper and CCD, and correction for the dark-current background, are performed in parallel on each of the four sub-images on each computer in ~1 s. During the calibration interval, the next data image is being collected. The 'flat-field' and 'mask' X-ray images required for the calibrations were collected only once, before the detector was installed at the NSLS, using the extended field produced by setting the detector far from the filtered point source of an Mo-target rotating-anode generator operating at various excitation voltages. The corrections for non-uniform response are accurate (preserve intensity information) to ~1%; the corrections for spatial distortion are accurate to 0.1 pixel. We have found that both corrections are time independent. The detector software converts the digitized CCD outputs into a corrected, seamless, 2048×2048 pixel image in the master computer.

We developed the software to merge seamlessly the four sub-images in order to preserve the accuracy of data near the taper interfaces, and to provide users with a visually continuous image. We have developed a detector control and display package that allows users to run the detector from Unix, Linux and Windows NT or 95 environments. At the NSLS, the detector is controlled through the *MARMAD* user interface (Skinner & Sweet, 1997). This program provides automatic dark-current image collection, data series image collection, wavelength selection *etc*. By writing image files in an appropriate format, a number of packages, including *DENZO*, *DPS*/*Mosflm* and *d*Trek* can be used for data reduction and analysis.

3. Characterization

3.1. Point response function

The point response function was measured by illuminating the detector face with a flood field of X-ray photons through a mask containing a set of pinholes each of size 20 μm, with the mask fixed to the Be entrance window. The radial profile of the average of 12 pinhole images is shown in Fig. 4. The FWHM of the PRF is 1.23 pixels (120 μm). The full width at 10, 1 and 0.1% of the maximum is 260, 410 and 810 μm, respectively.

3.2. Modulation transfer function

The modulation transfer function (MTF) was calculated from the line spread function (LSF). The LSF was measured using the tilted-slit method developed by Fujita *et al.* (1992). A Ta slit of width 40 μm was placed on the detector surface at an angle of ~1° with respect to the CCD pixel array. From the tilted-slit image one can generate the LSF sampled at spacings less than the Nyquest frequency. The Fourier transform of the LSF gives the one-dimensional MTF. Fig. 5 shows the measured LSF and the corresponding MTF.

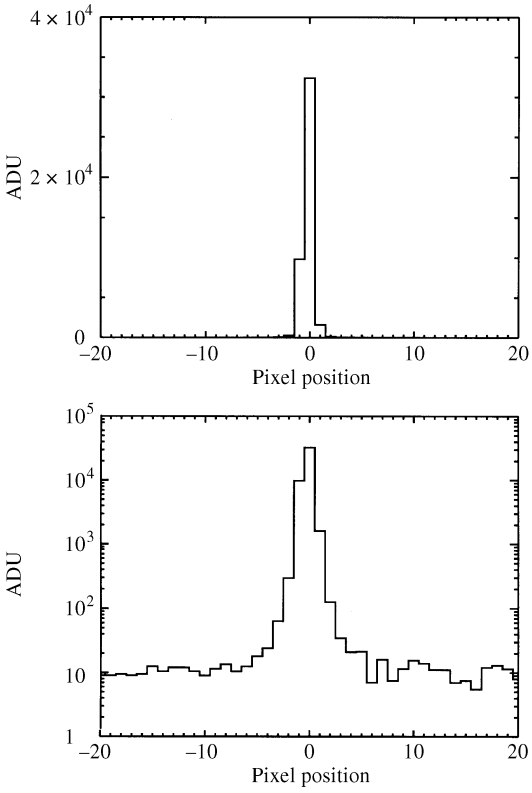

Figure 4
X-ray point response function (PRF) measured with a 20 μm pinhole, plotted on both a linear and a logarithmic scale.

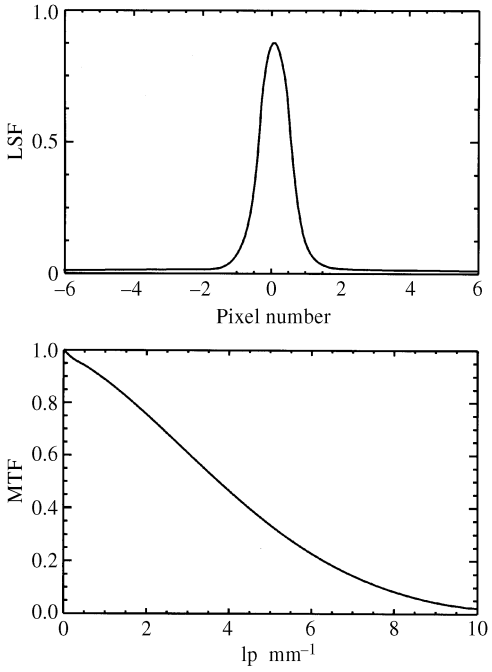

Figure 5
The measured line-spread function (LSF) and modulation transfer function (MTF).

3.3. Gain

The detector gain was measured by integrating the intensity in the (200) Bragg peak from an LiF crystal. The intensity (X-ray photons s^{-1}) in the peak was first measured with a calibrated NaI/photomultiplier counter. The gain [analog to digital units (ADU) per X-ray photon] was then determined with the detector by integrating the intensity (in ADU) in the peak. Due to the finite extent of the PRF and the profile of the Bragg peak, the gain is a function of the integration area. The gain for 8 keV X-ray photons is shown in Fig. 6 as a function of the integration radius. The gain in e ADU^{-1}, determined from the measured photon-transfer curve, is 7.0 e ADU^{-1} (Janesick *et al.*, 1985). For an integration radius of four pixels at 8 keV, the gain is 0.48 ADU per X-ray photon or 3.4 e per X-ray photon.

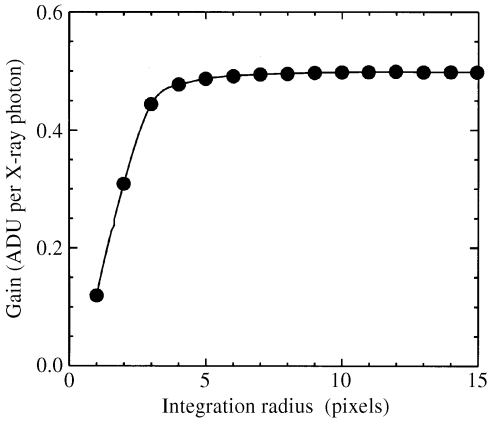

Figure 6
Effective gain measured as a function of the radius of integration of a Bragg peak for 8 keV X-ray photons.

3.4. Response linearity

The response of the detector to input X-ray photons was measured by collecting a series of images of X-ray absorbers illuminated by a constant-intensity X-ray flood field. The absorbers were made from several stacks of X-ray film. The exposure times for the series ranged from 2 to 200 s. The number of X-ray photons transmitted through the absorbers was determined with a calibrated NaI/photomultiplier counter. As shown in Fig. 7, the detector response is linear to within the uncertainty of our measurement (< 1%) over the entire range of intensity from background to nearly full well.

3.5. Noise

The contributions to the noise from the readout and the dark current were measured by taking sets of dark-current images with the CCD at 233 K for a series of integration times ranging from 2 to 100 s. The variance in the intensity at each pixel was calculated for each set of images. The average of these pixel variances, which is the combined variance of the readout and dark current for that period, is plotted in Fig. 8. The variance at $t = 0$ corresponds to the read noise, while the increase in the noise as a function of time results from the dark-current noise. From these data, the read-noise standard uncertainty per pixel is 1.8 ADU (12.6 e), and the dark current increases linearly at a rate of 0.052 ADU s^{-1} or 0.36 e s^{-1}. Thus, for a 30 s exposure with 1.0 Å X-ray photons, the standard uncertainty in the signal due to the read noise plus dark-current noise is equivalent to approximately three X-ray photons per pixel. In a typical crystallography experiment at the NSLS beamlines, the background from diffuse scattering from the sample and air scattering is considerably greater than

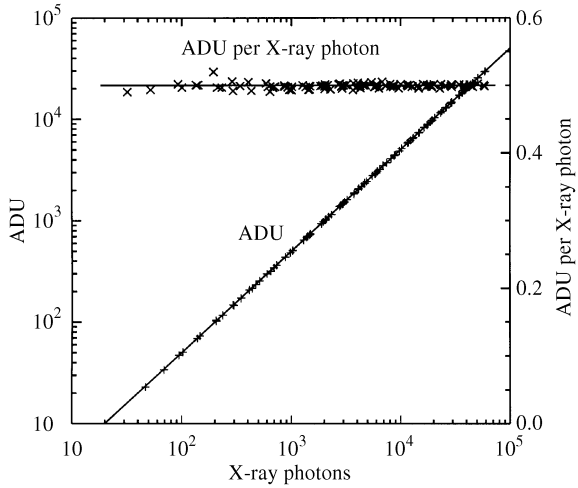

Figure 7
Linearity as a function of the number of 8 keV X-ray photons per pixel. The plot of ADU per X-ray photon (right-hand axis) shows that the response is linear over the range from 20 to 30 000 ADU. The ADU per X-ray photon scale has been normalized to 0.50 at 10^4 X-ray photons.

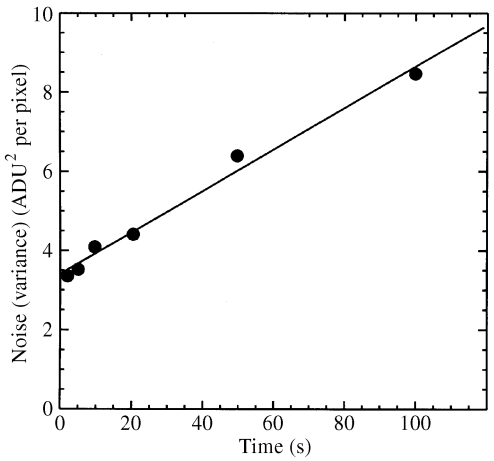

Figure 8
Variance (in ADU) in the signal per pixel, measured at 233 K without X-ray photons. The linear increase is due to the accumulation of dark-current signal in the CCD.

three X-ray photons per pixel in a 30 s exposure, so the detector noise makes a relatively small contribution to the measurement uncertainty.

3.6. Dynamic range

The effective dynamic range is determined by the maximum signal divided by the noise. The dynamic range can be determined for either a single pixel or a Bragg peak, for some integration interval. The detector response saturates at about 50 000 ADU per pixel; thus the dynamic range per pixel is 50 000/1.8 = 28 k for a zero-time integration interval and 50 000/2.55 = 20 k for a 60 s integration interval when the detector is operated at 233 K.

3.7. DQE

3.7.1. Predicted DQE for a Bragg peak. The quantum efficiency of each element in the signal chain, and the noise, can be used to predict the DQE of the detector. For a Bragg peak, the DQE as a function of the number of incident monochromatic X-ray photons (I) is given by (Stanton *et al.*, 1992):

$$\mathrm{DQE} = \frac{T_w}{1 + R_s + 1/G + A(n_R^2 + N_D t)/(IT_w G^2) + R_E T_w I}, \quad (1)$$

where T_w is the product of the window transmission (Be plus mylar) and phosphor absorption efficiency, R_s is the phosphor noise factor (typically $0.1 \leq R_s \leq 0.2$ for settled phosphors), G is the detector gain (e per X-ray photon), A is the peak integration area, n_R is the root mean square (r.m.s.) read noise, N_D is the dark-current rate, t is the integration time, and R_E is the relative variance contributed by other experimental conditions. The measured value of T_w at 1.54 Å is 0.86 (transmission of the Be is 0.935, transmission of the mylar is 0.935, absorption of the phosphor is 0.985). Using an integration radius of four pixels (which gives 95% of the full gain), the gain is 0.48 ADU per X-ray photon (3.4 e per X-ray photon). The integration radius of four pixels was chosen because it allows a high gain without including a large number of pixels. The more pixels included in the integration, the higher the noise. For weak peaks, a smaller integration radius could be used to increase the DQE. Using these parameter values and a readout noise of 1.8 ADU per pixel, a dark current of 0.052 ADU s^{-1} per pixel, setting R_s = 0.10 and setting the experimental variance $R_E = 25 \times 10^{-8}$, the predicted DQE for a Bragg peak for a 5 s exposure is given by

$$\mathrm{DQE}\,(1.54\,\text{Å}) = \frac{0.86}{1.40 + 887/I + (21.5 \times 10^{-8} I)}. \quad (2)$$

This predicted DQE is plotted in Fig. 9. Even in the absence of noise, the maximum value of the DQE is limited by absorption, the phosphor noise factor and the detector gain. Thus, the maximum DQE for any large-area CCD-based detector will generally be < 0.8.

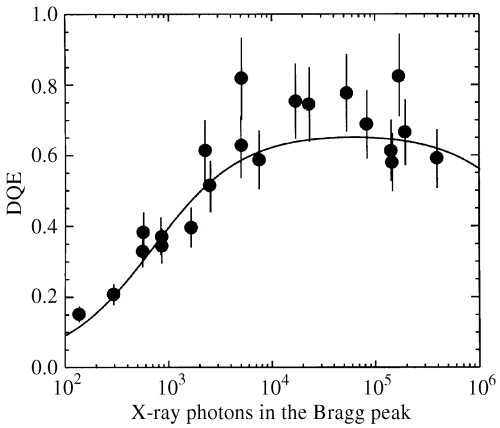

Figure 9
The DQE for a Bragg peak as a function of the number of X-ray photons in the peak for a 5 s integration time at a wavelength of 1.54 Å. Each data point was determined from 100 measurements of the intensity of a Bragg peak from an LiF crystal integrated in a four-pixel radius centered on the peak. The calculated curve is from equation (2).

3.7.2. Measurement of the DQE. The DQE was measured by collecting a series of 100 data frames of the image of a Bragg peak, and calculating the variance of the integrated intensity. In order to simulate crystallographic data-collection conditions, the incident beam was generated by a Cu-target rotating-anode X-ray tube, focused using bent mirrors and diffracted from an oriented LiF crystal using the (200) reflection (Phillips *et al.*, 1993). The focused 1.54 Å beam had an FWHM of 0.25 mm at the detector. The intensity of the beam was adjusted with calibrated absorbers and measured using an NaI-photomultiplier counter. The peak in the detector image was integrated over a radius of four pixels. The measured DQE as a function of the input X-ray intensity is plotted in Fig. 9. For a relatively weak peak with 500 X-ray photons, the DQE is ~0.35. For a peak with 10^4 X-ray photons, the DQE is ~0.7. The agreement between the measured and calculated DQE is reasonably close; the measured values are somewhat higher in the range between 10^4 and 10^5 X-ray photons in the peak.

4. Crystallographic results

The detector has been in operation since November 1997 at NSLS beamlines X12C and X25. In the first year of operation, 44 different research groups used the detector. Over 50 000 data images were collected in 350 complete data sets. For many of these, the crystal structures have been solved and published (Boriack-Sjodin *et al.*, 1998; Chen *et al.*, 1998; Golden *et al.*, 1998; Kim *et al.*, 1998; Conti *et al.*, 1998; Ban *et al.*, 1999; Spraggon *et al.*, 1998; Clemons *et al.*, 1999).

As a standard test of the detector, an anomalous difference Patterson map was calculated for data collected from a crystal of recombinant perdeutero wild-type sperm-whale myoglobin ($a = 34.5$, $b = 30.6$, $c = 63.7$ Å, $\beta = 105.5^\circ$), space group $P2_1$. The data were collected at a wavelength of 1.5 Å. Exposures were 10 s and the rotational increment was 1°. Ninety exposures were taken, the crystal was rotated 180°, and 90 more exposures were taken. The detector/diffractometer latency was about 3 s; the entire data collection took about 40 min. The Patterson function was calculated with data from 5 to 1.7 Å^{-1} resolution. The data were reduced with the *HKL* package (Otwinowski & Minor, 1997). The final merging R factor (on intensity) was 5.0%. The anomalous R-factor residual was 3.7% on F^2 and 2.3% on F. The difference Patterson function was calculated with the *PHASES* package (Furey & Swaminathan, 1997). Structure factors greater than 6σ were used. The ten largest differences were rejected as being potential outliers, and the 75% largest differences were employed. The peaks on the Harker section are 18 times the standard uncertainty of the map, and 19% of the origin peak. Plots of the Patterson map are shown in Fig. 10.

A data frame from a crystal with a large unit cell is shown in Fig. 11: a 300 s 1.5° rotation image from a crystal of the 50S ribosomal subunit, collected at 1.16 Å at beamline X12C [part of the work reported by Ban *et al.* (1998)]. Three points are illustrated in this image: (i) the background is dominated by scattering generated in the experiment; (ii) the peak width

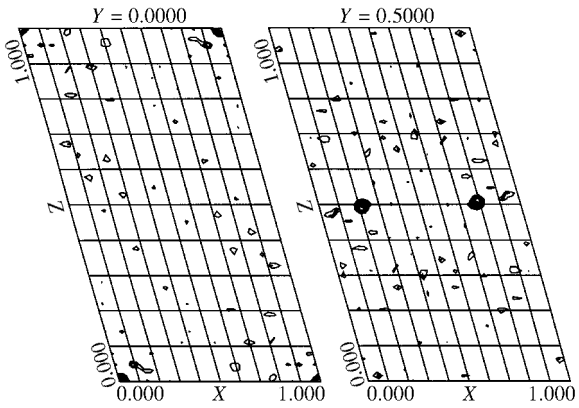

Figure 10
Anomalous difference Patterson map sections calculated for data collected from a crystal of perdeutero wild-type sperm-whale myoglobin, space group $P2_1$. The data set consisted of 180 1°-rotation 10 s exposures collected in 40 min at a wavelength of 1.5 Å at beamline X25. The Fe–Fe peaks are 18 times the standard uncertainty of the map, and 19% of the origin peak.

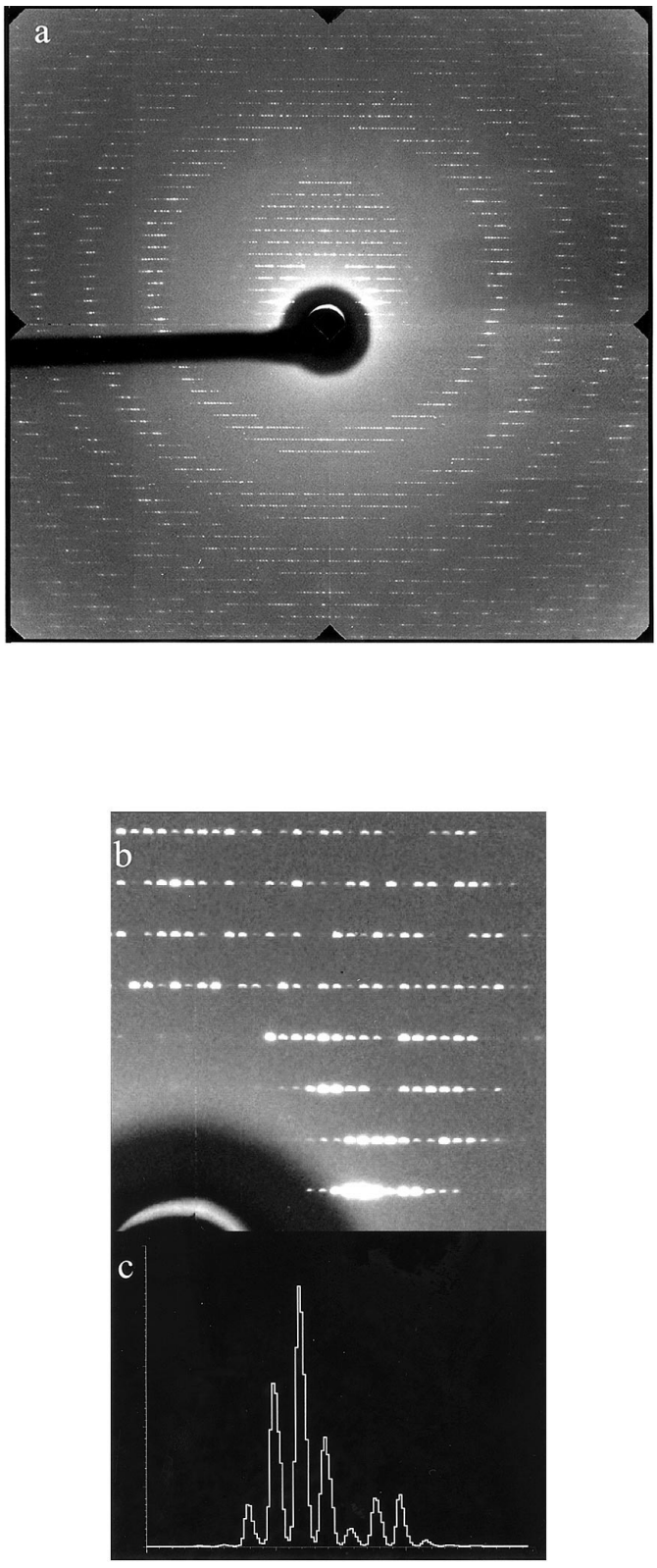

Figure 11
(*a*) Image from a 50S ribosomal subunit crystal, recorded with a wavelength of 1.16 Å, a rotation angle of 1.5°, exposure time of 300 s, and a crystal-to-detector distance of 500 mm. The *c*-axis unit-cell parameter is 575 Å. An area of this image near the beam stop is shown in (*b*) and a two-pixel-wide trace of the intensity through the centers of the peaks in the lower line of diffraction maxima is plotted in (*c*). The center-to-center distance in the trace is ~10 pixels.

(FWHM of four pixels) is determined primarily by the experiment, not the detector; (iii) Bragg peaks separated by 10 pixels (1 mm) can be accurately integrated.

5. Discussion

The design of the detector is based on our previous theoretical analysis of detector performance for macromolecular crystallography (Stanton, 1993; Stanton *et al.*, 1993). We endeavored to maximize the area of the detector by using four of the largest-area tapers available, coupled to 1 k × 1 k pixel, 24.6 mm CCDs, giving a 100 μm effective pixel size with a 4.1:1 taper demagnification. Because the loss in signal transmitted through the taper is proportional to the square of the demagnification, the consensus among detector builders when we started this project in 1993 was that the use of a 4:1 demagnification would seriously degrade performance. In order to maintain a relatively high DQE, we kept the detector electronic noise relatively low, but still kept the readout speed relatively fast by using four readout channels on each CCD. The readout noise per pixel is ∼2.5 equivalent 12 keV X-ray photons, and the full-image readout time is 1.6 s. We believe the performance results presented above justify our design choices.

The spatial resolution of the detector, plotted as the point response profile in Fig. 4, is determined mainly by light scattering in the converter, and to a lesser extent by light scattering in the taper. The 100 μm pixel size is commensurate with the PRF width of ∼120 μm FWHM (see Fig. 4). For macromolecular crystallography with focused-synchrotron or rotating-anode beams, the profile of Bragg peaks is typically 200–300 μm FWHM, determined by the size of the beam, the size of the crystal, the mosaic spread of the crystal, and the beam divergence. The inherent detector resolution is significantly less than the width of a Bragg peak, allowing a typical reflection to be adequately sampled. In most cases, at least 120 orders can be recorded on either side of the beam stop when the direct beam is centered on the detector. The pixel size could be reduced. For example, by using similar-sized CCDs with 2 k × 2 k pixels, one could achieve a 50 μm effective pixel size. Although this would allow finer spatial sampling, it might not improve the accuracy in the measurement of Bragg-peak integrated intensities. In fact, over-sampling a peak can decrease the measurement accuracy, because the integrated intensity would include the read noise from four times as many pixels, and the full-image readout time would become four times longer.

The agreement between the calculated and measured DQE in Fig. 9 shows that equation (1) models the performance of the detector relatively accurately. For typical integration times at synchrotron beamlines, the DQE is limited by electronic (read) noise only when the number of X-ray photons per pixel is very low. In the majority of crystallography data images made with this detector at the NSLS beamlines, the detector background, shown by the signal level behind the backstop and in the corners of the image, is significantly lower than the background elsewhere in the image (see Fig. 11). The phosphor noise, absorption and gain limit the DQE when the number of X-ray photons per pixel approaches 5×10^3.

At a synchrotron where frame times are often ∼10 s, we decided it would be important to keep the readout time less than 2 s, so that the duty cycle for a 10 s frame time would be >80%. As the readout speed increases, the read noise also increases. By using four readout channels per CCD and a 160 kHz channel readout speed (1.6 s total readout time), we attempted to balance these two considerations. In order to provide a fast frame-repeat rate, we optimized the speed of the calibration software. After the image on each CCD is read out, that image is fully calibrated in ∼1 s on the 200 MHz PC associated with that CCD. A new data frame can be collected (but not transferred to the PC) while the calibration calculations are taking place. Thus the maximum sustainable frame rate is ∼2.6 s.

The accuracy and time-independence of the response linearity and of the calibrations is demonstrated by the Patterson map from the myoglobin crystal (Fig. 10) and by the structures that have been solved.

Comparing the performance of this detector with that of the MAR imaging-plate detectors that were formerly installed on beamlines X12C and X25, we find that, on average, an equivalent data frame can be collected two to three times faster with the CCD detector than with the imaging-plate detectors. This is a direct result of the higher effective DQE of the CCD detector, and does not include any consideration of the longer readout time of the imaging-plate detectors.

We thank Dr V. Ramakrishnan and Dr F. Shu for providing the myoglobin crystal used to collect the anomalous difference Patterson data. Funding for this project was provided by the NSF grant BIR-9321872.

References

Ban, N., Freeborn, B., Nissen, P., Penczek, P., Grassucci, R. A., Sweet, R. M., Frank, J., Moore, P. B. & Steitz, T. A. (1998). *Cell*, **93**, 1105–1111.

Ban, N., Nissen, P., Hansen. J., Capel, M., Moore, P. & Steitz, T. A. (1999). *Nature (London)*, **400**, 841–847.

Boriack-Sjodin, P. A., Margarit, S. M., Bar-Sagi, D. & Kuriyan, J. (1998). *Nature (London)*, **394**, 337–343.

Chen, L., Glover, J. N. M., Hogan, P. G., Rao, A. & Harrison, S. C. (1998). *Nature (London)*, **392**, 42–48.

Clemons, W. M. Jr, May, J. L. C., Wimberly, B. T., McCutcheon, J. P., Capel, M. & Ramakrishnan, V. (1999). *Nature (London)*, **400**, 833–840.

Conti, E., Uy, M., Leighton, L., Globel, G. & Kuriyan, J. (1998). *Cell*, **94**, 193–204.

Fujita, H., Tsai, D., Itoh, T., Doi, K., Morishita, J., Ueda, K. & Ohtzuka, A. (1992). *IEEE Trans. Med. Imag.* **II** 1, 34–39.

Furey, W. & Swaminathan, S. (1997). *Methods in Enzymology*, Vol. 277B, *Macromolecular Crystallography*, edited by C. W. Carter & R. M. Sweet, p. 590. New York: Academic Press

Golden, B. L., Gooding, A. R., Podell, E. R. & Cech, T. R. (1998). *Science*, **282**, 259–265.

Gruner, S. M., Barna, S. L., Wall, M. E., Tate, M. W. & Eikenberry, E. (1993). *Proc. Soc. Photo-Opt. Instrum. Eng.* **2009**, 98–108.

Janesick, J., Klaasen, K. & Elliott, T. (1985). *Proc. Soc. Photo-Opt. Instrum. Eng.* **570**, 7–12.
Kim, H., Xia, D., Yu, C. A., Xia, J. Z., Kachurin, A. M., Zhang, L., Yu, L. & Deisenhofer, J. (1998). *Proc. Natl Acad. Sci. USA*, **95**, 8026–8033.
Naday, I., Ross, S., Kayno, M., Westbrook, M. L., Westbrook, E., Phillips, W. C., Stanton, M. & O'Mara, D. (1995). *Proc. Soc. Photo-Opt. Instrum. Eng.* **2415**, 236–249.
Naday, I., Westbrook, E. M., Westbrook, M. L., Travis, D. J., Stanton, M., Phillips, W. C., O'Mara, D. & Xie, J. (1994). *Nucl. Instrum. Methods A*, **348**, 635–640.
Otwinowski, Z. & Minor, W. (1997). *Methods in Enzymology*, Vol. 276A, *Macromolecular Crystallography*, edited by C. W. Carter & R. M. Sweet, p. 307. New York: Academic Press.
Phillips, W. C., Li, Y., Stanton, M., Xie, J. & O'Mara, D. (1993). *Nucl. Instrum. Methods A*, **334**, 621–630.
Skinner, J. M. & Sweet, R. M. (1997). *Acta Cryst.* D**54**, 718–725.
Spraggon, G., Applegate, D., Everse, S. J., Zhang, J.-Z., Veerapandian, L., Redman, C., Doolittle, R. F. & Grieninger, G. (1998). *Proc. Natl Acad. Sci. USA*, **95**, 9099–9104.
Stanton, M. (1993). *Nucl. Instrum. Methods A*, **325**, 550–557.
Stanton, M., Phillips, W., Li, Y. & Kalata, K. (1992). *J. Appl. Cryst.* **25**, 638–645.
Stanton, M., Phillips, W. C., O'Mara, D., Naday, I. & Westbrook, E. (1993). *Nucl. Instrum. Methods A*, **325**, 558–567.
Stanton, M., Phillips, W. C. & O'Mara, D. (1994). *Soc. Photo-Opt. Instrum. Eng.* **2278**, 16–20.
Suzuki, M., Yamamoto, M., Kumasaka, T., Sato, K., Totokawa, H., Aries, I. F., Jerram, P. A., Gullick, D. & Ueki, T. (1999). *J. Synchrotron Rad.* **6**, 6–18.
Tate, M. W., Eikenberry, E. F., Barna, S. L., Wall, M. E., Lowrance, J. L. & Gruner, S. M. (1995). *J. Appl. Cryst.* **28**, 196–205.